J. Fluid Mech. (2014), *vol.* 746, *pp.* 606–625.
doi:10.1017/jfm.2014.139

Fractional dynamics of tethered particles in oscillatory Stokes flows

Edwin A. Lim[1], Marcelo H. Kobayashi[2] and Carlos F. M. Coimbra[1,†]

[1]Department of Mechanical and Aerospace Engineering, Jacobs School of Engineering, University of California, San Diego, La Jolla, CA 92093, USA

[2]Department of Mechanical Engineering, College of Engineering, University of Hawaii at Mānoa, Honolulu, HI 96822, USA

(Received 28 June 2013; revised 12 January 2014; accepted 9 March 2014)

A mechanistic model for the low-Reynolds-, high-Strouhal-number behaviour of a system consisting of a spherical particle attached to an inelastic tether under uniform sinusoidal cross-flow is presented. Unsteady history drag and virtual mass effects are considered for both the sphere and the tether. The mechanics of the problem is such that the resulting coupled fractional differential equations are linear and solvable analytically. The stationary solutions obtained in this work show that there are limiting dimensions for the length and thickness of the tether when compared to the radius of the particle that allow for the motion of the particle–tether system to simulate the motion of a free particle. These conditions exist for the range of small oscillation amplitudes that are required for keeping the particle Reynolds number smaller than unity while oscillating the particle–tether system at high frequencies (Strouhal numbers larger than unity). The fractional order model for the particle–tether system is compared against detailed experimental results for tethered particles for a wide range of experimental frequencies, including the low-frequency range where tether effects are measurable.

Key words: multiphase and particle-laden flows, multiphase flow, particle/fluid flow

1. Introduction

The motion of a free particle in oscillatory Stokes flow is a classical problem in fluid mechanics for which a wealth of theoretical results exist (Hjelmfelt & Mockros 1966; Chao 1968; Hinze 1975; Morrison & Stewart 1976). Expanding on the work of Boussinesq (1885) and Basset (1888), Tchen (1947) produced an equation to describe the motion of a spherical particle in an unbounded uniform flow. The high-frequency dynamics of a small particle in a viscous fluid is of obvious importance in turbulent dispersion flows where the monomodal frequency response to Stokes flows represents a reasonable model for particle–flow interactions when the Kolmogorov length scale is of the same order of magnitude or larger than the particle radius (see e.g. Coimbra & Rangel 2001; Hwang & Eaton 2006). In the particular regime of small particle Reynolds number ($Re_p = aU_0/\nu < 1$, where U_0 is the relative velocity, a is the particle radius and ν is the kinematic viscosity) and high Strouhal number ($Sl = a\Omega/9U_0 > 1$,

† Email address for correspondence: ccoimbra@ucsd.edu

where Ω is the angular frequency of oscillation), both experimental and theoretical results show that Basset (history) drag effects are substantial, surpassing in magnitude the combined effects of steady Stokes drag and virtual mass forces (Coimbra & Rangel 2001; Coimbra *et al.* 2004; L'Espérance *et al.* 2005).

There has been a number of recent attempts to characterize low-Reynolds-number particle–flow interactions at the range of frequencies that corresponds to $S = Sl\,Re_p = a^2\Omega/9\nu \sim 1$ (see e.g. Abbad & Souhar 2004; Candelier, Angilella & Souhar 2004; L'Espérance *et al.* 2006; Candelier & Souhar 2007; Weinstein, Kassoy & Bell 2008) for non-neutrally buoyant particles. Because the objective is to study the particle response to flow accelerations, the gravitational migration of non-neutrally buoyant particles results in a number of experimental difficulties. Souhar and collaborators studied various rotating and steady shear flow configurations for free settling particles and bubbles, while Coimbra and collaborators opted to cancel the particle force along the gravitation direction by tethering the particle to a fluid container (see Coimbra *et al.* 2004 for a detailed description of the experimental apparatus). While the tether option has yielded very accurate high-frequency measurements (L'Espérance *et al.* 2005, 2006), questions remained about the effect of the tether on the motion of the particle, particularly at lower frequencies. This work addresses the dynamics of the particle–tether system by formulating the problem from first principles. A direct determination of the fractional order of the history drag from experimental results for low-Reynolds-number particle motion is also presented, and the order is validated for a wide range of physical parameters, more specifically for the regime given by dimensionless local accelerations equal to or larger than unity ($Sl\,Re_p \geqslant 1$).

2. Physical model for the particle–tether system

Consider a dynamic system consisting of a particle of radius a that is connected to the end of a tether of length L and radius r; see figure 1(*a*). The other extremity of the tether is connected to a solid wall that oscillates in tandem with the uniform background flow of $U(T) = U_0 e^{i\Omega T}$. The tether prevents a light particle from floating to the top of the fluid cell and the heavy particles from sinking to the bottom. With the particles restrained from moving vertically, the fluid cell is vibrated harmonically in the horizontal plane. The domain is two-dimensional because the resulting hydrodynamic forces that act on both the particle and the tether are confined to the X–Y plane. This oscillation induces a response from the particle–tether system. We denote by $X_t(Y, T)$ and $X_p(T)$ the horizontal displacements of the tether and the centroid of the particle, respectively. For an oscillation amplitude that is sufficiently small compared to the length of the tether, we can disregard the vertical motion of the particle–tether system. However, we consider the tension in the tether, Υ, which is a result of the density difference between the particle and the fluid. Thus, we derive two equations of motion, one for the particle and one for the tether. It should be noted that although the forces acting on the particle and tether are three-dimensional in nature, the motions can be completely described in two dimensions.

The equation of motion for the particle is a modified version of Tchen's equation (Tchen 1947) for a solid sphere in accelerating Stokes flow. With the position of the particle on the x-axis at T represented by $X_p(T)$, the equation of motion is then

$$m_p \frac{\mathrm{d}^2 X_p}{\mathrm{d}T^2} = m_f \frac{\mathrm{D}U}{\mathrm{D}T} - \frac{m_f}{2}\left(\frac{\mathrm{d}^2 X_p}{\mathrm{d}T^2} - \frac{\mathrm{D}U}{\mathrm{D}T}\right) - \Lambda_p\left(\frac{\mathrm{d}X_p}{\mathrm{d}T} - U\right) - \frac{a\Lambda_p}{\sqrt{\nu}}\tilde{\mathcal{D}}^{1/2}\left(\frac{\mathrm{d}X_p}{\mathrm{d}T} - U\right) - \Upsilon \sin\theta. \tag{2.1}$$

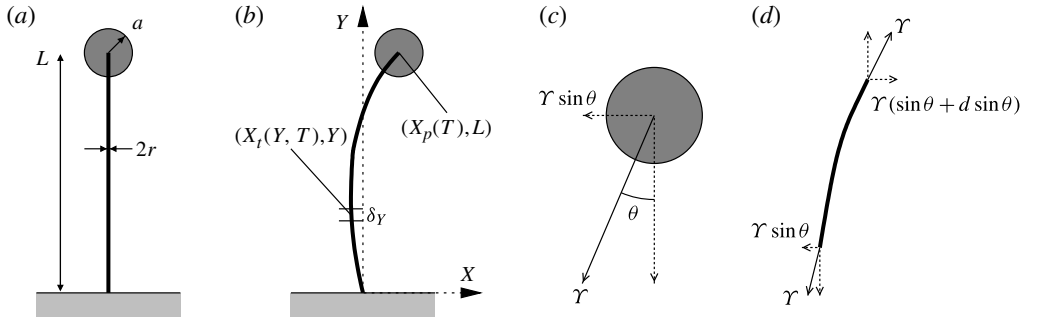

FIGURE 1. Particle–tether system: (*a*) quiescent position, showing key dimensions; (*b*) swaying under forcing; (*c*) tension components on the particle; (*d*) tension components on the elemental tether δ_Y. The base of the tether is attached to the fluid cell, which oscillates sinusoidally. Here $X_t(Y, T)$ is the shape of the tether, and $X_t(0, T)$ refers to the base of the tether, which moves with the fluid cell, whereas $X_t(L, T)$ refers to the other tether extremity, so that $X_t(L, T) = X_p(T)$.

Here $m_p = (4/3)\pi a^3 \rho_p$ and $m_f = (4/3)\pi a^3 \rho_f$ are, respectively, the masses of the particle and the displaced fluid, and $\Lambda_p = 6\pi\mu a$ is the Stokes drag coefficient for a sphere. Note that for uniform background flow, $\mathrm{D}U/\mathrm{D}T = \mathrm{d}U/\mathrm{d}T$; however, for completeness, we have written the above equation using $\mathrm{D}U/\mathrm{D}T$. The first four terms on the right-hand side of the equation are pressure, added mass force, Stokes drag and Basset history drag (Basset 1888). The history drag takes the usual form for high-Strouhal-, low-Reynolds-number flows so that for a given steady drag $\Lambda_p \boldsymbol{V}$, the history drag is $a\Lambda_p \nu^{-1/2} \tilde{\mathcal{D}}^{1/2}(\boldsymbol{V})$, where $\tilde{\mathcal{D}}^{1/2}(\boldsymbol{V})$ represents the half-derivative of the particle velocity (Coimbra & Rangel 1998). The Caputo definition of the generalized differential operator is (Podlubny 1999)

$$\tilde{\mathcal{D}}^q \boldsymbol{V} = \frac{1}{\Gamma(p-q)} \int_{-\infty}^{T} \frac{\mathrm{d}\boldsymbol{V}(\sigma)}{\mathrm{d}\sigma} (T-\sigma)^{p-q-1} \, \mathrm{d}\sigma, \tag{2.2}$$

where $\Gamma(s)$ is the gamma (generalized factorial) function of s, and $p - 1 \leqslant q < p$. Here p is the smallest integer larger than q, e.g. if $q = 1/2$ then $p = 1$. The last term on the right-hand side of (2.1) is an addition to Tchen's original equation of motion, representing the lateral component of the tether tension $\Upsilon \sin\theta$. This tension component serves as the coupling to the equation for the tether, and can be approximated by $\Upsilon \, \partial X_t/\partial Y$ for small θ; see figure 1(*c*). With the small-angle approximation, the equation of particle motion can then be linearized as

$$\begin{aligned} m_p \frac{\mathrm{d}^2 X_p}{\mathrm{d}T^2} = {} & m_f \frac{\mathrm{D}U}{\mathrm{D}T} - \frac{m_f}{2}\left(\frac{\mathrm{d}^2 X_p}{\mathrm{d}T^2} - \frac{\mathrm{D}U}{\mathrm{D}T}\right) - \Lambda_p \left(\frac{\mathrm{d}X_p}{\mathrm{d}T} - U\right) \\ & - \frac{a\Lambda_p}{\sqrt{\nu}} \tilde{\mathcal{D}}^{1/2}\left(\frac{\mathrm{d}X_p}{\mathrm{d}T} - U\right) - \Upsilon \left.\frac{\partial X_t}{\partial Y}\right|_{Y=L}. \end{aligned} \tag{2.3}$$

We assume that the tether is thin enough that the traverse shear component is negligible, i.e. only axial tension is considered. Furthermore, the tension is taken to be constant throughout the tether and equal to the net buoyancy force of the particle alone, so $\Upsilon = (m_f - m_p)G_c$ where $G_c = 9.81$ m s^{-2}. For a tether with a linear specific

mass of k (kg m^{-1}), the momentum principle applied to a vertical element, δ_Y, of the tether yields

$$k\delta_Y \frac{\partial^2 X_t}{\partial T^2} = -\Lambda_t \left(\frac{\partial X_t}{\partial T} - U\right)\delta_Y - \frac{\Lambda_t r}{\sqrt{\nu}}\tilde{\mathcal{D}}^{1/2}\left(\frac{\partial X_t}{\partial T} - U\right)\delta_Y - \rho_f \pi r^2 \left(\frac{\partial^2 X_t}{\partial T^2} - 2\frac{\mathrm{D}U}{\mathrm{D}T}\right)\delta_Y + \Upsilon \frac{\partial(\sin\theta)}{\partial Y}\delta_Y. \tag{2.4}$$

Here $X_t(Y, T)$ thus describes the shape of the tether. The viscous drag coefficient for a cylinder in cross-flow is

$$\Lambda_t = \frac{4\pi\mu}{\ln\epsilon_r - 1/2} = \frac{4\pi\mu}{f(\epsilon_r)}, \tag{2.5}$$

with $\epsilon_r = L/r$ being the geometric ratio (see Sherman 1990, p. 275). The first and second terms in the right-hand side of (2.4) are the steady and history drag forces acting on the tether (see e.g. Coimbra & Rangel 1998; Coimbra & Kobayashi 2002). Next is the virtual mass force. The differential in the lateral component of the tension (figure 1(*d*)) completes the equation.

After cancelling the δ_Y factors in all terms and linearizing the angular displacement, we arrive at

$$k\frac{\partial^2 X_t}{\partial T^2} = -\Lambda_t \left(\frac{\partial X_t}{\partial T} - U\right) - \frac{\Lambda_t r}{\sqrt{\nu}}\tilde{\mathcal{D}}^{1/2}\left(\frac{\partial X_t}{\partial T} - U\right) - \rho_f \pi r^2 \left(\frac{\partial^2 X_t}{\partial T^2} - 2\frac{\partial U}{\partial T}\right) + \Upsilon \frac{\partial^2 X_t}{\partial Y^2}. \tag{2.6}$$

The boundary conditions for the tether are

$$\left.\frac{\partial X_t}{\partial T}\right|_{Y=0} = U_0 \mathrm{e}^{\mathrm{i}\Omega T} \tag{2.7}$$

and

$$X_t(L, T) = X_p(T). \tag{2.8}$$

The former represents the end of the tether that is attached to the cell and is therefore oscillating along with the cell (fluid). The latter equation states that the end of the tether is attached to the centroid of the particle. Note that although the formulation and illustration seem to assume that the particle is lighter than the fluid ($\rho_p < \rho_f$) and hence positioned at the top end of the tether with the tether itself affixed to the cell at the bottom end, the resulting equations are valid for heavy particles ($\rho_p > \rho_f$) as well. The only difference is that the tether is attached to the ceiling of the fluid cell for heavy particles.

2.1. *Non-dimensionalization*

Both equations of motion and their boundary conditions are non-dimensionalized with the velocities scaled by U_0 and time scaled by $\tau_p = 2a^2/(9\nu\alpha_p)$. The dimensionless number $\alpha_p = \rho_f/\rho_p$ is the fluid-to-particle density ratio. Two different length scales are used for the x- and y-axes, and they are, respectively, $U_0\tau_p$ and L. Denoting non-dimensional variables by lowercase letters, the equation for the particle becomes

$$\ddot{x}_p = \alpha_p \dot{u} - \frac{\alpha_p}{2}\left(\ddot{x}_p - \dot{u}\right) - \left(\dot{x}_p - u\right) - \left(\frac{9}{2}\alpha_p\right)^{1/2}\mathcal{D}^{1/2}\left(\dot{x}_p - u\right) - \left(\alpha_p - 1\right) g\, x_t'\big|_{y=1}, \tag{2.9}$$

where $g = G_c \tau_p^2 / L$ is the dimensionless gravitational acceleration, $\mathcal{D}$ is the dimensionless generalized differential operator with respect to time, while prime represents partial derivative with respect to y and overdot represents time derivative.

The dimensionless form of the tether equation is

$$\ddot{x}_t = -\alpha_t (\ddot{x}_t - 2\dot{u}) - \frac{8}{9} \frac{1}{f(\epsilon_r)} \frac{\alpha_t}{\alpha_p} \left(\frac{\epsilon_r}{\epsilon_a} \right)^2 (\dot{x}_t - u) - \frac{8}{9} \frac{1}{f(\epsilon_r)} \frac{\alpha_t}{\alpha_p} \left(\frac{9}{2} \alpha_p \right)^{1/2} \frac{\epsilon_r}{\epsilon_a} \mathcal{D}^{1/2} (\dot{x}_t - u) + \frac{4}{3} (\alpha_p - 1) \frac{\alpha_t}{\alpha_p} \left(\frac{\epsilon_r}{\epsilon_a} \right)^2 \frac{g}{\epsilon_a} x_t'', \tag{2.10}$$

with $\alpha_t = \rho_f / \rho_t$ being the fluid–tether density ratio and $\epsilon_a = L/a$ the ratio of tether length to particle radius. The corresponding boundary conditions are

$$\dot{x}_t(0, t) = u(t) = \mathrm{e}^{\mathrm{i}\omega t} \tag{2.11}$$

and

$$x_t(1, t) = x_p(t). \tag{2.12}$$

2.2. *Solution*

The resulting formulation is a coupled linear partial differential equation system with constant coefficients that represents the dynamics of the particle and the tether. Note that the fractional derivative operators do not alter the linearity of the system (Coimbra 2003). Because we are interested only in the stationary solution, initial conditions are not relevant. The stationary solution has an oscillatory component with the same frequency as the flow; accordingly, we propose a separable solution of the form

$$x_t(y, t) = \chi(y) \mathrm{e}^{\mathrm{i}\omega t}, \tag{2.13}$$

where the time component matches the fluid oscillation $u(t)$. The homogeneous solution vanishes for $t \to \infty$ because it is associated with the constants of integration that must be determined from the initial conditions, and initial conditions do not play a role in stationary effects. Nevertheless, the family of homogeneous solutions is important since it will affect the particular solution.

When the order of derivatives is fractional, the family of homogeneous solutions is no longer exponential. Instead they are Mittag–Leffler functions which are defined as

$$E_m(z) = \sum_{n=0}^{\infty} \frac{z^n}{\Gamma(mn + 1)}. \tag{2.14}$$

In the particular case of (2.10), where the fractional order is 1/2, the family of homogeneous solutions is

$$E_{1/2} \left(\lambda_i \sqrt{t} \right) = \mathrm{e}^{\lambda_i^2 t} \mathrm{erfc} \left(-\lambda_i \sqrt{t} \right), \tag{2.15}$$

with appropriate eigenvalues λ_i. Since this $E_{1/2}(\lambda_i \sqrt{t})$ family of homogeneous solutions is not represented by a linear combination of terms in $\mathrm{e}^{\mathrm{i}\omega t}$, the choice of (2.13) as the particular solution is justified. Because the forcing function also has the oscillatory form $\mathrm{e}^{\mathrm{i}\omega t}$, the particular solution represents the stationary solution for the system.

Substitution of the boundary condition (2.12) along with the appropriate derivatives of x_t and u into the particle equation gives us, after cancelling $e^{i\omega t}$ and some manipulation,

$$\chi'(1) + \frac{1}{(\alpha_p - 1)g}\left[-\left(1 + \frac{\alpha_p}{2}\right)\omega^2 + \left(\frac{9}{2}\alpha_p\right)^{1/2} e^{i3\pi/4}\omega^{3/2} + i\omega\right]\chi(1)$$
$$= \frac{1}{(\alpha_p - 1)g}\left[i\frac{3}{2}\alpha_p\omega + \left(\frac{9}{2}\alpha_p\right)^{1/2} e^{i\pi/4}\omega^{1/2} + 1\right] \tag{2.16}$$

or, in a simpler form with suitable M and N,

$$\chi'(1) + M\chi(1) = N. \tag{2.17}$$

Note that the semi-derivatives are

$$\mathcal{D}^{1/2}\left(\dot{x}_p\right) = e^{i3\pi/4}\omega^{3/2}\chi(1)e^{i\omega t} \tag{2.18}$$

and

$$\mathcal{D}^{1/2}(u) = e^{i\pi/4}\omega^{1/2}e^{i\omega t}. \tag{2.19}$$

Applying similar treatment to the equation for the tether yields

$$\chi'' - \frac{3}{4}\frac{\epsilon_a}{(\alpha_p - 1)g}\left[-\left(\frac{1 + \alpha_t}{\alpha_t}\right)\alpha_p\left(\frac{\epsilon_a}{\epsilon_r}\right)^2\omega^2\right.$$
$$\left. + \frac{8}{9}e^{i3\pi/4}\frac{1}{f(\epsilon_r)}\left(\frac{9}{2}\alpha_p\right)^{1/2}\frac{\epsilon_a}{\epsilon_r}\omega^{3/2} + i\frac{8}{9}\frac{1}{f(\epsilon_r)}\omega\right]\chi$$
$$= -\frac{3}{4}\frac{\epsilon_a}{(\alpha_p - 1)g}\left[i2\alpha_p\left(\frac{\epsilon_a}{\epsilon_r}\right)^2\omega + \frac{8}{9}e^{i\pi/4}\frac{1}{f(\epsilon_r)}\left(\frac{9}{2}\alpha_p\right)^{1/2}\frac{\epsilon_a}{\epsilon_r}\omega^{1/2} + \frac{8}{9}\frac{1}{f(\epsilon_r)}\right]. \tag{2.20}$$

Thus the tether equation is a second-order ordinary differential equation (ODE) in χ. The original particle equation (2.9) combines with the original boundary equation (2.11) to form a mixed boundary condition for χ at $y = 1$. The other boundary equation (2.12) is

$$\chi(0) = -\frac{i}{\omega} \tag{2.21}$$

after integration. Using appropriate substitutions, we can rewrite (2.20) as

$$\chi'' - \beta^2\chi = B. \tag{2.22}$$

Furthermore, with the transformation of $\zeta'' = \chi''$ and $\zeta = \chi + B/\beta^2$, the original ODE becomes homogeneous in ζ, i.e.

$$\zeta'' - \beta^2\zeta = 0, \tag{2.23}$$

which, for constant coefficients, has the general solution

$$\chi = \zeta - \frac{B}{\beta^2} = c_1e^{\beta y} + c_2e^{-\beta y} - \frac{B}{\beta^2}. \tag{2.24}$$

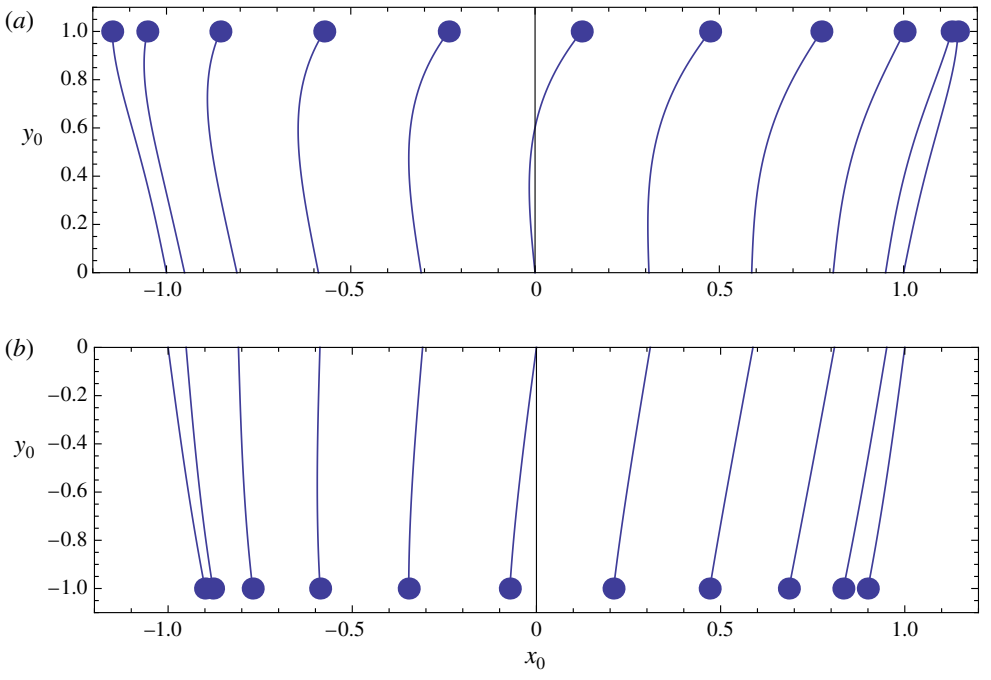

FIGURE 2. (Colour online) Composite frames of the fluid cell travelling a distance of one amplitude from left to right for 10 even time intervals for: (*a*) a light particle, with $\alpha_p = 2$; (*b*) a heavy particle, with $\alpha_p = 0.5$. The other parameters for the two particles are identical: $\omega = 1$, $\alpha_t = 1$, $\epsilon_a = 10$, $\epsilon_r = 10^3$ and $g = 0.1183$. The particle disc is only representative and is not proportionally sized to either scale. The y-axis is normalized by the length of the tether L, so that $y_o = y/L$, whereas the x-axis is normalized by the fluid cell displacement Δx, i.e. $x_o = x/\Delta x$. The x-axis scale is dilated to the order of $\epsilon_a = 10^3$ with respect to the y-axis for clarity (for $Re_p < 1$ and $Sl\,Re_p \sim 1$, $\Delta x < a$).

The constants of integration are then

$$c_1 = \frac{N + M\dfrac{B}{\beta^2} + \left(\dfrac{B}{\beta^2} - \dfrac{\mathrm{i}}{\omega}\right)(\beta - M)\,\mathrm{e}^{-\beta}}{(\beta + M)\,\mathrm{e}^{\beta} + (\beta - M)\,\mathrm{e}^{-\beta}} \tag{2.25}$$

and

$$c_2 = -c_1 + \frac{B}{\beta^2} - \frac{\mathrm{i}}{\omega}. \tag{2.26}$$

3. Results and discussion

Figure 2 illustrates the motion of both a light particle and a heavy particle. The particle is represented by the disc at one end of the tether. The other end of the tether is either anchored to the floor of the cell in the case of a light particle or suspended from the ceiling in the case of a heavy particle. Hence, the tether end that is attached to the cell represents the motion of the fluid. For the light particle, note that the particle has a larger oscillation amplitude than the cell. This figure also shows, by the inflection of the rightmost tether, that the light particle has already started on the 'return' trip in advance of the fluid. The x-axis is scaled by the particle radius and the y-axis is scaled by the tether length.

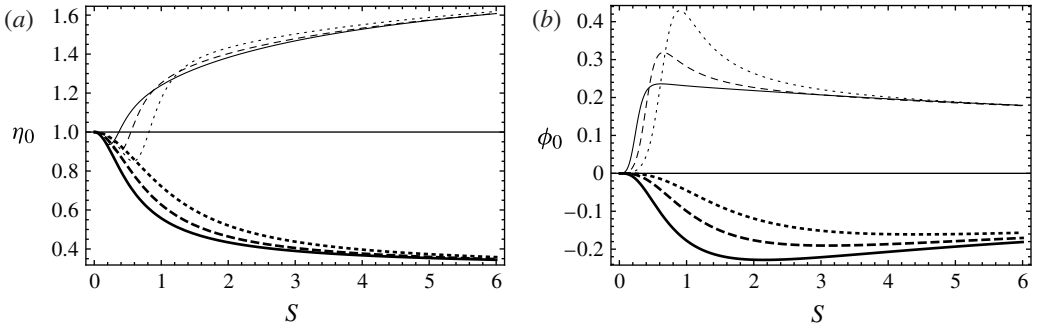

FIGURE 3. Effect of varying tether length on: (*a*) the ratio of the particle oscillation magnitude to the fluid displacement; (*b*) the phase offset of the particle with respect to the fluid cell. Thin lines (dotted, dashed and solid) represent a light particle with $\alpha_p = 5$, and thick lines represent a heavy particle with $\alpha_p = 0.2$. Dotted lines correspond to the baseline length of $\epsilon_a = 5$, dashed lines correspond to two times the baseline length, and solid lines correspond to four times the baseline length. The other parameters are $\omega = 1$, $\alpha_t = 1$, $\epsilon_r = 1000$ and $\tau_p = 0.0278$.

3.1. *Dominating effect of the length of the tether*

The addition of the tether to the particle system introduces three additional parameters, namely the length, thickness and density of the tether. A dimensional analysis for this system yields the parameters ϵ_r, ϵ_a and α_t that are interconnected in the solution for χ, which is itself composed of several terms. However, (2.9) shows that the tether affects the motion of the sphere through the horizontal component of the tension, which depends on the total tension and the slope of the tether at the attachment point. The total tension represents the upper bound on the tether effect, although the assumption of a small angle θ in the analysis means that the solution is not applicable long before large tether deflections are reached. Hence, the slope of the tether, by virtue of the assumption of small deflection, always has limited influence on the particle motion. The assumption of small deflection is not really restrictive in this case, because the amplitude oscillations that satisfy $Re_p < 1$ are necessarily smaller than a, so the slope deflection of the tether is always small as long as the length of the tether is many times larger than the radius of the particle.

On the other hand, the total tension $(\alpha_p - 1)g = (\alpha_p - 1)G_c\tau_p^2/L$ contains only the length of the tether as a parameter. Clearly, the larger the tether, the lesser its effect on the motion of the particle. The tension effect varies approximately as $O(1/L)$ for a long tether. In the case of very long tethers, the particle motion essentially becomes decoupled from the tether motion because the angular deflection for small-amplitude vibrations is very small in comparison to the length of the tether (see figure 3).

The effect of the tether on the particle increases when the tether is small in comparison to the radius of the particle and when the density of either is substantially different from that of the fluid. In such cases, the shape of the tether becomes important due to the nonlinear coupling between the tether and the particle motion. This effect is accentuated at larger-amplitude oscillations, especially for lower S values, even when the fluid cell oscillations are smaller than the radius a of the particle.

Amplitude and phase offset comparisons are accomplished by using the fluid cell (and therefore the background flow) as a reference. The amplitude ratio is defined

mathematically as

$$\eta_0 = \frac{|\chi(1)|}{|\chi(0)|}, \tag{3.1}$$

and the phase offset as

$$\phi_0 = \arg[\chi(1)] - \arg[\chi(0)]. \tag{3.2}$$

Note that for the fluid, $\arg[\chi(0)] = -\pi/2$.

When the particle is heavier than the fluid ($\alpha_p < 1$), it oscillates less than the fluid cell ($\eta_0 < 1$). A heavy particle also *lags* the fluid ($\phi_0 < 0$). The opposite is true when the particle is lighter than the fluid. As a direct consequence of the virtual mass and pressure forcing effects, a lighter particle has a larger oscillation amplitude than the fluid (up to three times larger). A lighter particle also *leads* the fluid since virtual mass effects account for a sign change in acceleration before the sign change in velocity occurs.

3.1.1. *Weak dependence on tether thickness and density*

From the discussion above, one would expect the thickness (ϵ_r) and density (α_t) of the tether to have minor influence on the particle motion. This position is supported by figure 4, which shows that even varying those parameters significantly makes little difference to the amplitude ratio and phase offset for the entire range of parameters. For the experimentalist, this is advantageous because the parameter that affects the system the most, i.e. the length of the tether, is easy to adjust. Adjusting the thickness and density of the tether is usually much more difficult.

3.2. *Comparison with the motion of untethered particles*

For a free (untethered) particle, we solve for the quasi-steady solution using (2.3) without including the tether tension term. The solution in dimensionless form that is consistent with the tethered particle is

$$x_f(t) = \chi_f e^{i\omega t}, \tag{3.3}$$

where

$$\chi_f = \frac{i\frac{3}{2}\alpha_p\omega + e^{i\pi/4}\left(\frac{9}{2}\alpha_p\right)^{1/2}\omega^{1/2} + 1}{-\left(1+\frac{\alpha_p}{2}\right)\omega^2 + e^{i3\pi/4}\left(\frac{9}{2}\alpha_p\right)^{1/2}\omega^{3/2} + i\omega}. \tag{3.4}$$

A more complete analysis of free-particle motion in harmonic Stokes flows is given in Coimbra & Rangel (2001). Employing a similar approach to the fluid comparison, we compare the oscillation amplitude ratio and phase offset of the tethered particle with those of the free particle. Hence,

$$\eta_f = \frac{|\chi(1)|}{|\chi_f|} \tag{3.5}$$

and

$$3.5\phi_f = \arg[\chi(1)] - \arg\left[\chi_f\right]. \tag{3.6}$$

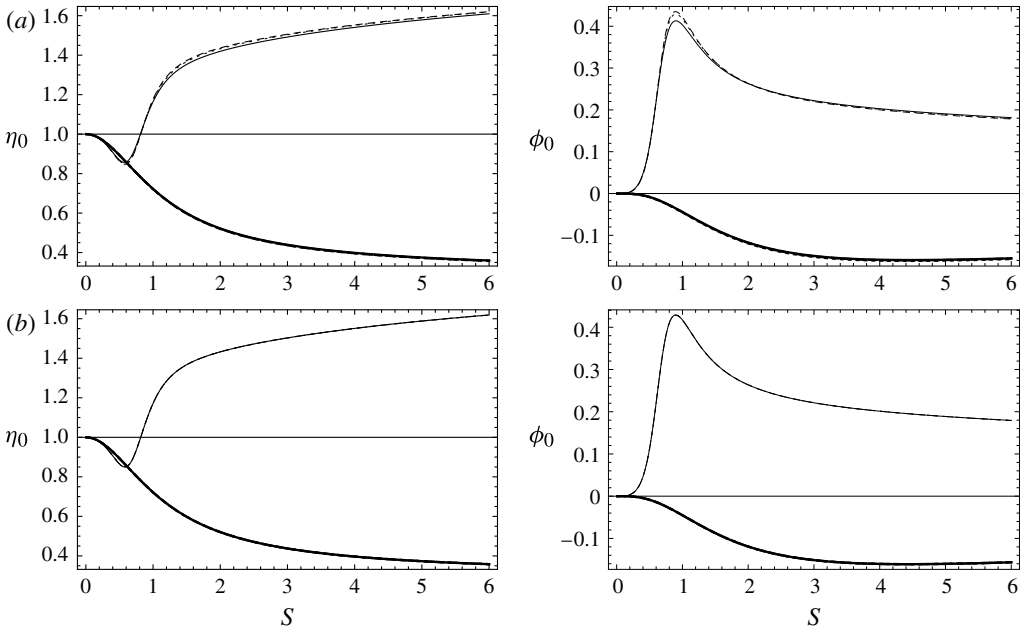

FIGURE 4. Tether thickness (ϵ_r) and density (α_t) have almost no influence on the particle motion: (*a*) dotted lines correspond to a tenth of the baseline thickness, and dashed lines correspond to 10 times the baseline thickness; (*b*) dotted lines correspond to a fifth of the baseline density, and dashed lines correspond to five times the baseline density. The plots are relative to the fluid motion in both oscillation magnitude and phase angle. Thin lines represent light particles ($\alpha_p = 5$) and thick lines represent heavy particles ($\alpha_r = 0.2$). Solid lines represent the baseline values of $\omega = 1$, $\epsilon_a = 5$, $\epsilon_r = 1000$, $\alpha_t = 1$ and $\tau_p = 0.0278$.

Figure 5 corroborates the previous observation that the longer the tether, the smaller the effect on the particle.

3.3. *Contribution of each individual force*

The particle equation of motion (2.3) accounts for all the main forces acting on the particle. These forces include pressure (term), added mass force, Stokes drag, Basset drag and tension. In this subsection, we determine the relative importance of each type of force on the resulting motion for different flow parameters.

To complement the discussion of the previous section, we compare the free-particle solution with the case of no history effects, i.e. the solution that does not consider the Basset history drag, to single out the effects of the Basset force. Thus, we consider

$$\chi_{\bar{f}} = \frac{\mathrm{i}\,\dfrac{3}{2}\alpha_p\omega + 1}{-\left(1 + \dfrac{\alpha_p}{2}\right)\omega^2 + \mathrm{i}\omega}. \tag{3.7}$$

Figure 6 shows that consideration of Basset drag can be more important to the particle amplitude displacement and phase offset than the effect of the tether for the given parameters.

In general, for each force i, we have

$$F_i = |F_i|\,\mathrm{e}^{\mathrm{i}\theta_i}, \tag{3.8}$$

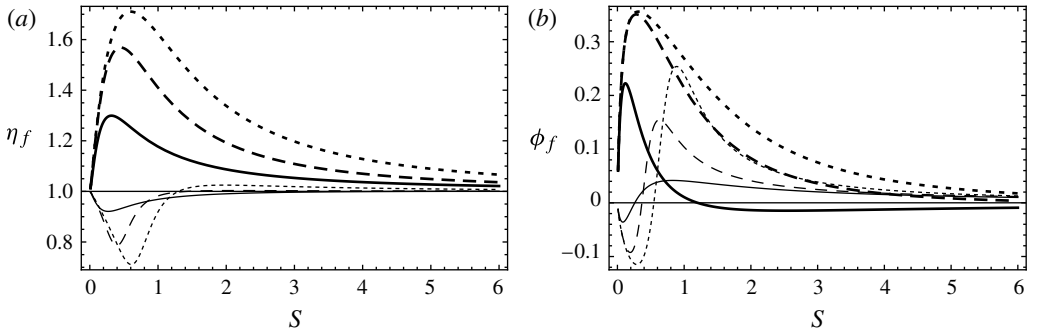

FIGURE 5. Motion of a tethered particle in comparison to a free particle: (*a*) the particle-to-fluid amplitude ratio; (*b*) the phase offset between the particle and the fluid. Thin lines (dotted, dashed and solid) represent a light particle with $\alpha_p = 5$, and thick lines represent a heavy particle with $\alpha_p = 0.2$. Dotted lines correspond to the baseline length of $\epsilon_a = 5$, dashed lines correspond to two times the baseline length, and solid lines correspond to four times the baseline length. The other parameters are $\omega = 1$, $\alpha_t = 1$, $\epsilon_r = 1000$ and $\tau_p = 0.0278$, as in figure 3.

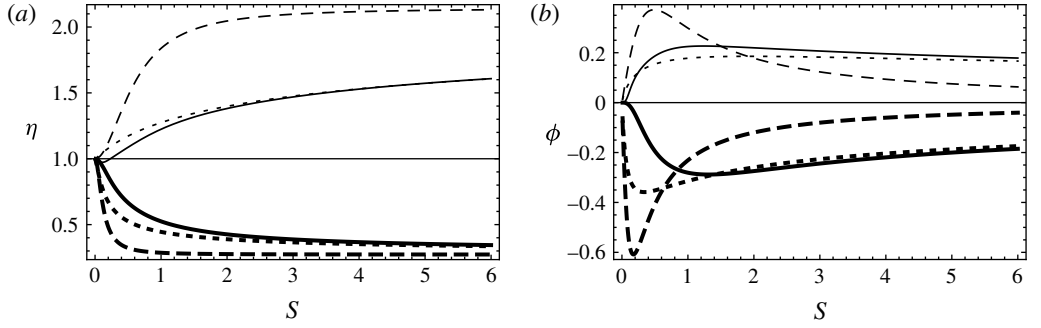

FIGURE 6. Comparison of a tethered particle, a free particle, and a free particle sans Basset drag: (*a*) amplitude ratio; (*b*) phase offset. All amplitudes and phase offsets are calculated with respect to the fluid displacement and phase. The solid lines represent a tethered particle, the dotted lines represent a free particle, and the dashed lines represent a free particle without Basset drag. As before, thin lines represent a light particle with $\alpha_p = 5$ and thick lines represent a heavy particle with $\alpha_p = 0.2$. The rest of the parameters are $\omega = 1$, $\alpha_t = 1$, $\epsilon_a = 50$, $\epsilon_r = 1000$ and $\tau_p = 0.0278$.

where $\theta_i = \arg(F_i)$ is the complex argument. For example, the Stokes drag in (2.9) is

$$-\left(\dot{x}_p - u\right) = -\left[\mathrm{i}\omega\chi(1)\mathrm{e}^{\mathrm{i}\omega t} - \mathrm{e}^{\mathrm{i}\omega t}\right] = -\left[\mathrm{i}\omega\chi(1) - 1\right]\mathrm{e}^{\mathrm{i}\omega t}, \tag{3.9}$$

so $F_{Stokes} = \mathrm{i}\omega\chi(1) - 1$. The resultant force on the particle is then $F_{tot} = \sum F_i$. The fractional contribution of each force type would be

$$f_i = \frac{|F_i|\cos(\theta_{tot} - \theta_i)}{|F_{tot}|}. \tag{3.10}$$

Figure 7 shows the contribution from the different forces as they act along the direction of the resultant force. It is clear that the effect of the tether is strongly

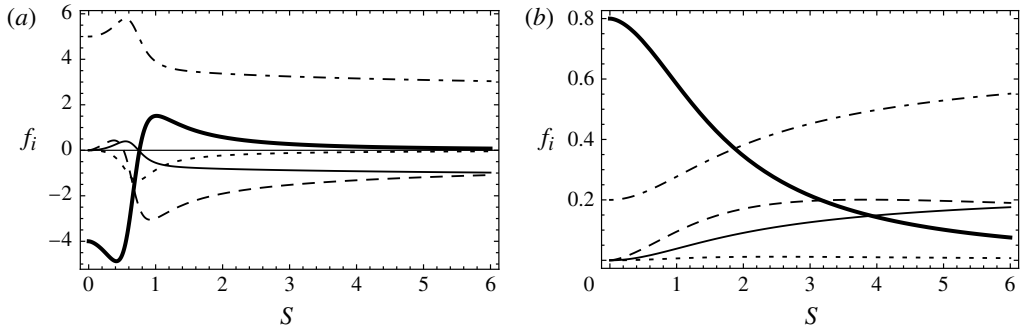

FIGURE 7. Relative contribution of the various forces as a component of the resultant force (3.10): (*a*) a light particle with $\alpha_p = 2$; (*b*) a heavy particle with $\alpha_p = 0.5$. The dot–dashed lines represent pressure, the thin solid lines added mass force, the dotted lines Stokes drag, the dashed lines Basset drag and the thick solid lines tension. The other parameters are $\omega = 1$, $\alpha_t = 1$, $\epsilon_r = 10^3$, $\epsilon_a = 10$ and $g = 0.1183$.

dependent on the parameters chosen, and even on the frequency range. For the light particle, the tether force is dominant for low values of S, but goes through a minimum at $S \approx 0.8$, and then changes sign and goes through another local maximum for $S \approx 1$. Although the relative contribution of the tether tension force changes with the parameters, in all cases tether effects are less important for higher values of S. The Basset drag, virtual mass and pressure term have substantial influence on the particle throughout the experimental frequency range. After reaching a maximum for S slightly below unity for light particles, the Basset drag decays slowly for $S \gg 1$. The relative behaviour of the forces for S in the approximate range 0.6–0.8 reflects the fact that the Stokes drag, the Basset drag, the pressure–virtual mass term and the tether are out of phase with each other, and the total force acting on the particle reaches a minimum at this range for the given parameters. For light particles, the shape of the tether is more complex due to the fact that the displacements are larger with larger phase offsets (light particles 'lead' the fluid by a larger amount than heavy particles 'lag' the fluid), and this complexity of the tether shape is reflected in the projection of the tether tension on the resultant force. It is also relevant to point out that the projection of the force alone throughout the harmonic cycle does not translate into a direct effect on the measurable values of amplitude displacement and phase offset due to the fact that other forces may cancel individual force contributions. Also, a larger projection on the resultant when the magnitude of the resultant is itself larger has less effect on the amplitude displacement and phase offset than a larger relative projection when the resultant is small.

Previous works studied the relative importance of the forces that depend directly on the relative velocity $(\dot{x_p} - u)$ (see e.g. Chao 1968; Morrison & Stewart 1976; Coimbra & Rangel 2001) for a free particle under zero gravitational effects. In those comparisons, the Basset drag reaches its relative maximum contribution in respect to the virtual mass and the Stokes drag forces at $S = 1$, while the acceleration-dependent forces (virtual mass) dominate for $S \gg 1$ and the velocity-dependent Stokes drag is dominant at low frequencies. However, other forces that are not directly dependent on the relative velocity play a critical role at different frequency ranges. Figure 7 shows that, at very low frequencies, the tether is the dominant force, and is the only force that can balance the pressure forcing term. All forces asymptote to zero for $S \to 0$,

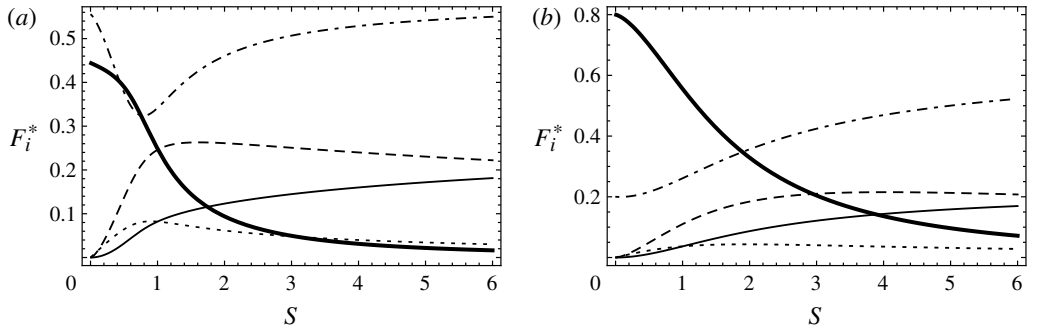

FIGURE 8. Relative contribution of the magnitude of each force normalized by the sum of all force magnitudes, i.e. (3.11): (*a*) a light particle with $\alpha_p = 2$; (*b*) a heavy particle with $\alpha_p = 0.5$ The dot–dashed lines represent pressure, the thin solid lines added mass force, the dotted lines Stokes drag, the dashed lines Basset drag and the thick solid lines tension. The other parameters are $\omega = 1$, $\alpha_t = 1$, $\epsilon_r = 10^3$, $\epsilon_a = 10$ and $g = 0.1183$.

but the relative contributions of the dominant forces in this limit are amplified by the normalization used in (3.10), which forces the sum of the individual forces to equal unity.

Instead of considering the component of the forces along the direction of the resultant force normalized by the magnitude of the resultant, if we consider the magnitude of the forces normalized by the sum of the absolute contributions as

$$F_i^* = \frac{|F_i|}{\sum |F_i|}, \tag{3.11}$$

this allows us to depict the relative contributions of the individual forces normalized by the sum of the magnitudes, as shown in figure 8.

Figures 7 and 8 provide the experiment designer with a clear picture of the magnitudes of the individual forces for cases where the tether tension is relatively important. They also provide information critical to the design of experiments that rely on tethers to counteract gravitational effects. For instance, if the goal of the experiment is to reflect free-particle motion, the experiments should be conducted with $\epsilon_r > 10^3$ and be limited to values of $S > 1$, particularly if heavy particles are used. If the objective of the experiments is to study history (Basset) effects on free-particle motion (which are maximized for values of $S \sim 1$), experimental errors induced by the tether are minimized for very large values of ϵ_r using light particles, for which the forces are greater in magnitude and both the displacement and the phase offset are much larger than for heavy particles. This is particularly important because the phase offset between the Stokes drag and Basset drag is only $\pi/4$, which is also the phase offset between the Basset drag and the virtual mass force. In order to minimize experimental uncertainty, both the amplitude displacement and the phase offset should be maximized, which can be achieved by using the maximum value of α_p. Following the same rationale, if the goal is to study tether effects, experiments should be conducted for $S \sim 1$, light particles and moderately high values of ϵ_r (recall that the theory presented here is valid only for $\epsilon_r \gg 1$).

3.4. *Comparison with experimental data*

L'Espérance *et al.* (2005) presented detailed experimental results of the particle–tether system for particles of various sizes and densities. The experiments were performed

in a heavy lubricant fluid (DuPont Krytox, $\rho_f = 1.84$ g cm^{-3}) with very thin copper wires as tethers ($\rho_t = 8.93$ g cm^{-1}, $L = 25$ mm and $2r = 19$ μm), giving the tether parameters $\alpha_t = 0.2060$ and $\epsilon_r = 2632$. The experimental set-up for the results presented in L'Espérance *et al.* (2005) was an evolution of the experimental set-up used by Coimbra *et al.* (2004) to study particle history effects for the regime $Re_p < 0.5$ and $Sl > 1$ and for the range $0.015 < S = Sl\,Re_p < 5$. Although covering a wider range of parameters, the experiments reported in Coimbra *et al.* (2004) were characterized by relative errors of the order of 5–20 % for heavy particles and smaller than 5 % for light particles. Most of the high-value errors occurred for smaller values of S, with particularly high errors occurring for heavy particles in the $0.1 < S < 0.5$ range. The larger errors were attributed to three different causes: (i) at low-frequencies ($S < 1$), the electromagnetic shaker was unable to produce a monomodal sinusoidal oscillation; (ii) due to their higher inertia, heavy particles displace less, which compromises the accuracy of the particle position estimation by the holographic set-up; and (iii) tether effects are likely to play a role in the low-S range, as shown in figure 5. Furthermore, the low-Re_p high-Sl assumption breaks down as values of S drop much below unity. To circumvent these issues, and because the goal of the experiments performed by L'Espérance *et al.* (2005) was to measure history effects precisely, a more controlled experimental set-up with a redesigned voice coil for the electromagnetic shaker was used, and only values taken at higher frequencies ($S > 1$) were reported. This was done to ensure that tether effects were negligible, with the overall result that the effects of the Basset force were measured with accuracies never reported before or since (relative errors smaller than 1 %).

However, since the present work focuses on the effects of the tether, experimental results at low values of S are more relevant. Figure 9 shows a comparison with experimental data that includes not only the values reported by L'Espérance *et al.* (2005) but also data points for S values slightly below unity. The dashed lines represent the free-particle model, while the solid lines represent the tethered-particle model. It is clear that the tethered model results agree strongly with the experimental data for the whole range of $S > 1$ when tether effects are small because of the relatively long tether, and also for values of S less than unity when tether effects should be measurable according to the model proposed in this work. The effect of considering the tether in the formulation is more clearly seen in figure 10, which is an amplification of figure 9 for the cases where a larger amplitude ratio and phase offset can be measured. The tethered-particle model more accurately reflects the experimental results for values of S as low as 0.5.

To quantify the results, we define the mean deviation and root mean square error associated with the amplitude ratio η to be

$$\bar{\sigma}_\eta = \frac{1}{n}\sum \left(\eta_{expr} - \eta_{predict}\right) \tag{3.12}$$

and

$$RMSE_\eta = \sqrt{\frac{1}{n}\sum \left(\eta_{expr} - \eta_{predict}\right)^2}, \tag{3.13}$$

respectively, where n is the number of samples. Comparison with experiments yields $\bar{\sigma}_\eta = 0.0055$ and $RMSE_\eta = 0.0104$ for the amplitude displacement. Similar treatment of the phase offset data yields $\bar{\sigma}_\phi = -0.0005$ and $RMSE_\phi = 0.0108$.

Figure 11 shows that the Basset force plays a dominant role in determining the motion of the styrofoam particle when $S > 1$, and in fact is only smaller in

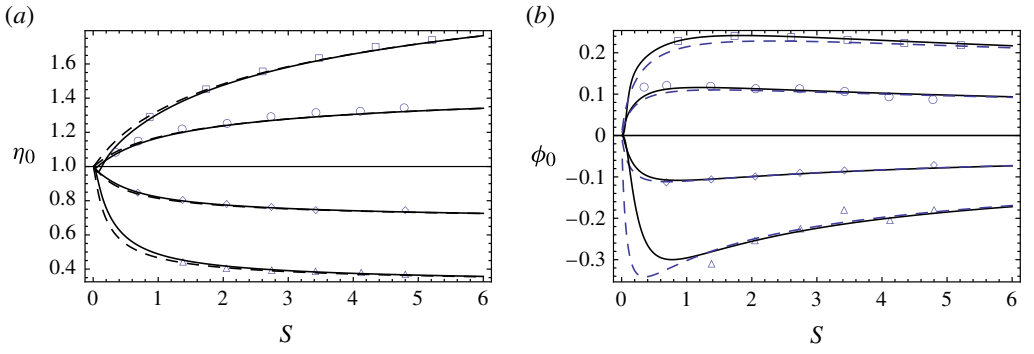

FIGURE 9. (Colour online) Experimental results compared to analytical predictions for the particle–tether system: (*a*) amplitude ratio; (*b*) phase offset. Solid lines correspond to a theoretical tethered particle, and dashed lines correspond to a free (untethered) particle. The fixed parameters for all data sets are $\alpha_t = 0.2060$ and $\epsilon_r = 2632$. The different particles are: styrofoam with $\alpha_p = 13.14$, $\epsilon_a = 11.21$ and $g = 0.00173$ (squares); polypropylene with $\alpha_p = 2.14$, $\epsilon_a = 12.62$ and $g = 0.04066$ (circles); silicon nitride with $\alpha_p = 0.563$, $\epsilon_a = 12.62$ and $g = 0.5879$ (diamonds); and brass with $\alpha_p = 0.214$, $\epsilon_a = 12.62$ and $g = 4.075$ (triangles). Error bars are roughly of the same dimension as the symbols. Note that the experimental results for $S > 1$ correspond to the values reported by L'Espérance *et al.* (2005).

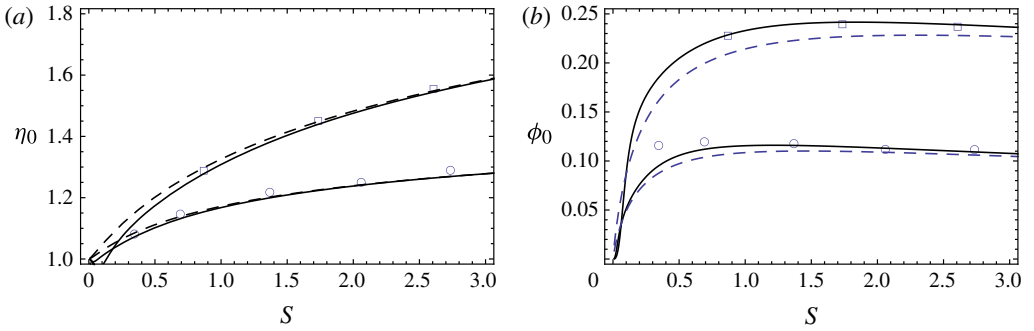

FIGURE 10. (Colour online) Experimental results compared to analytical predictions for the particle–tether system: (*a*) amplitude ratio; (*b*) phase offset. Solid lines correspond to a theoretical tethered particle, and dashed lines correspond to a free particle. The fixed parameters for all data sets are $\alpha_t = 0.2060$ and $\epsilon_r = 2632$. The different particles are: styrofoam with $\alpha_p = 13.14$, $\epsilon_a = 11.21$ and $g = 0.00173$ (squares); and polypropylene with $\alpha_p = 2.14$, $\epsilon_a = 12.62$ and $g = 0.04066$ (circles). Tether effects are noticeable for $S \sim 1$, especially in the phase offset, but decay fast for $S > 1$.

magnitude than the pressure term over most of the experimental range of frequencies for styrofoam and polypropylene particles. Tether effects decay very fast for $S > 0.5$ but are very important for $S < 0.2$ in the case of styrofoam particles; however, they are not noticeable for the denser polypropylene particles.

3.5. *On the kernel of the history force term*

Coimbra & Rangel (1998) showed that in the limit of infinitesimal particle Reynolds number ($Re_p \to 0$) and for Strouhal number much larger than unity ($Sl \gg 1$), the

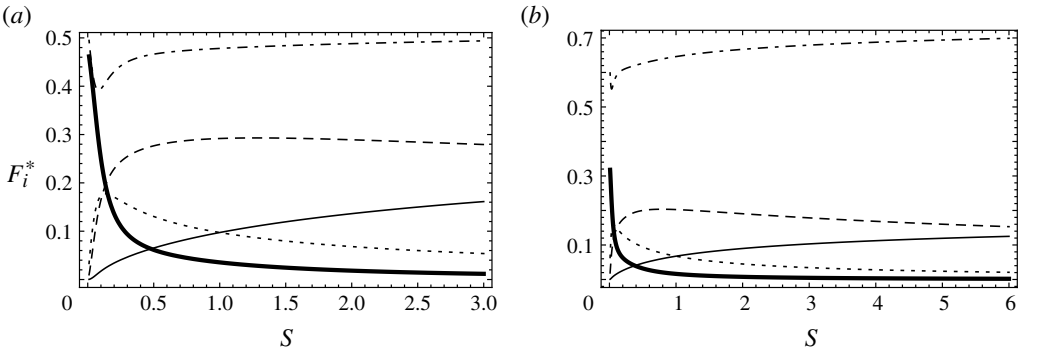

FIGURE 11. Force fractions (as defined by (3.11)) for the two different types of light particle: (*a*) styrofoam with $\alpha_p = 13.14$, $\epsilon_a = 11.21$ and $g = 0.00173$; (*b*) polypropylene with $\alpha_p = 2.14$, $\epsilon_a = 12.62$ and $g = 0.04066$. The fixed parameters for all data sets are $\alpha_t = 0.2060$ and $\epsilon_r = 2632$.

history (Basset) drag, which is normally written in integral form, can be represented exactly by a semi-derivative (i.e. of order 1/2). The fractional formulation reflects the fact that the Basset drag is mathematically equal to a semi-derivative differential operator applied to the steady Stokes drag, which results in a term that carries the same coefficient Λ_p of the steady Stokes drag times the square root of the diffusion time ($a\sqrt{\nu}$) as in (2.3).

While there is no controversy about the validity of the Basset kernel for high Strouhal numbers ($Sl \gg 1$), even for Re_p slightly larger than unity, there has been substantial research devoted to the low-frequency or long-term decay of the history force (see e.g. Mei, Lawrence & Adrian 1991; Mei & Adrian 1992; Kim, Elghobashi & Sirignano 1998). Numerical simulations of oscillatory flow past a fixed sphere (Mei & Adrian 1992; Pedro *et al.* 2008) and of freely moving particles (Kim *et al.* 1998) have provided insight into the functional form of the history kernel at low and high frequencies and at both very low and moderate Re_p ranges. With the detailed model for the particle–tether system developed in this work, we are in a position to evaluate the range of values for which the order of the Basset term is equal to 1/2, and to verify directly from the experiments whether the theoretical value of the order of the derivative is applicable to the whole range of experimental values, which includes a few experiments for values of $S = Sl\,Re_p \leqslant 1$.

Let $W = \mathrm{d}X_p/\mathrm{d}T - U$ represent the relative velocity in the equation of motion for the particle, (2.3); then the Stokes drag is simply

$$6\pi\mu a W, \tag{3.14}$$

whereas the Basset drag has the form

$$6\pi\mu\frac{a^2}{\nu}\tilde{\mathcal{D}}^{1/2}W, \tag{3.15}$$

with $6\pi\mu a = \Lambda_p$ as mentioned above. Using L, M and T to denote length, mass and time dimensions, the dimensions of the Stokes drag, LMT^{-2}, must be the same as the dimensions of $a\nu^{-1/2}\tilde{\mathcal{D}}^{1/2}W$ from the Basset drag. This is true if the semi-derivative $\tilde{\mathcal{D}}^{1/2}$ has the dimension of $T^{-1/2}$, as is the case. However, if there are deviations in

the order of the kernel for the history force (see e.g. Kim *et al.* 1998; Pedro *et al.* 2008), a more generic form for the Basset drag can be expressed as

$$6\pi\rho_f a^m \nu^n \tilde{\mathcal{D}}^q W, \tag{3.16}$$

where the values of m and n are determined through dimensional analysis and validated by experiments. Here we assume that ρ_f has an exponent of unity, since this is the only physical parameter that includes mass as a dimension, and the mass dimension must have an exponent to be compatible with the Stokes drag ($6\pi\nu\rho_f aW$). Once more, the dimensions of $a^m\nu^n\tilde{\mathcal{D}}^q W$ must match the dimensions of νaW (L^4T^{-2}) from the Stokes drag, or

$$L^m \left(L^2T^{-1}\right)^n T^{-q} \left(L^1T^{-1}\right) = L^{m-2n+1}T^{n-1-q} = L^4T^{-2}. \tag{3.17}$$

Matching the exponents and solving for m and n as functions of q, we arrive at $m = 1+2q$ and $n = 1-q$. We conclude that the Basset drag with undetermined order is

$$6\pi\rho_f a^{1+2q}\nu^{1-q}\tilde{\mathcal{D}}^q W = \Lambda_p \left(\frac{a^2}{\nu}\right)^q \tilde{\mathcal{D}}^q W. \tag{3.18}$$

With this Basset drag form, the equation of motion for the particle is

$$\begin{aligned} m_p \frac{\mathrm{d}^2X_p}{\mathrm{d}T^2} \;=\; & m_f \frac{\mathrm{D}U}{\mathrm{D}T} - \frac{m_f}{2}\left(\frac{\mathrm{d}^2X_p}{\mathrm{d}T^2} - \frac{\mathrm{D}U}{\mathrm{D}T}\right) - \Lambda_p\left(\frac{\mathrm{d}X_p}{\mathrm{d}T} - U\right) \\ & - \Lambda_p \left(\frac{a^2}{\nu}\right)^q \tilde{\mathcal{D}}^q \left(\frac{\mathrm{d}X_p}{\mathrm{d}T} - U\right) - \Upsilon \left.\frac{\partial X_t}{\partial Y}\right|_{Y=L}. \end{aligned} \tag{3.19}$$

Using similar analysis, the counterpart generic equation for the tether is

$$\begin{aligned} k\delta_Y \frac{\partial^2 X_t}{\partial T^2} \;=\; & -\Lambda_t\left(\frac{\partial X_t}{\partial T} - U\right)\delta_Y - \Lambda_t\left(\frac{r^2}{\nu}\right)^q \tilde{\mathcal{D}}^q\left(\frac{\partial X_t}{\partial T} - U\right)\delta_Y \\ & - \rho_f \pi r^2 \left(\frac{\partial^2 X_t}{\partial T^2} - 2\frac{\mathrm{D}U}{\mathrm{D}T}\right)\delta_Y + \Upsilon \frac{\partial^2 X_t}{\partial Y^2}\delta_Y. \end{aligned} \tag{3.20}$$

Non-dimensionalization of the particle equation of motion results in

$$\ddot{x}_p = \alpha_p \dot{u} - \frac{\alpha_p}{2}\left(\ddot{x}_p - \dot{u}\right) - \left(\dot{x}_p - u\right) - \left(\frac{9}{2}\alpha_p\right)^q \mathcal{D}^q\left(\dot{x}_p - u\right) - \left(\alpha_p - 1\right) g\, x_t'\big|_{y=1}, \tag{3.21}$$

and the tether equation can be written as

$$\begin{aligned} \ddot{x}_t \;=\; & -\alpha_t\left(\ddot{x}_t - 2\dot{u}\right) - \frac{8}{9}\frac{1}{f(\epsilon_r)}\frac{\alpha_t}{\alpha_p}\left(\frac{\epsilon_r}{\epsilon_a}\right)^2\left(\dot{x}_t - u\right) \\ & - \frac{8}{9}\frac{1}{f(\epsilon_r)}\frac{\alpha_t}{\alpha_p}\left(\frac{\epsilon_r}{\epsilon_a}\right)^2\left(\frac{\epsilon_a}{\epsilon_r}\right)^{2q}\left(\frac{9}{2}\alpha_p\right)^q \mathcal{D}^q\left(\dot{x}_t - u\right) \\ & + \frac{4}{3}\left(\alpha_p - 1\right)\frac{\alpha_t}{\alpha_p}\left(\frac{\epsilon_r}{\epsilon_a}\right)^2 \frac{g}{\epsilon_a} x_t''. \end{aligned} \tag{3.22}$$

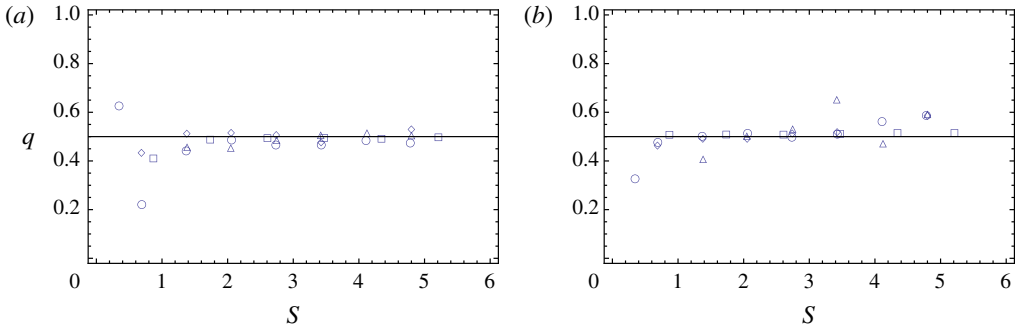

FIGURE 12. (Colour online) The order of the Basset derivative, q, is calculated inversely from the experimental data to determine the unknown q that satisfies the amplitude and phase equations. Each marker corresponds to results solved numerically using the secant method: (*a*) q values that satisfy the experimental results for the amplitude ratio, with a mean deviation of -0.0245 with respect to $q = 1/2$ and a corresponding root mean square error of 0.0689. (*b*) q values obtained experimentally from phase offsets, which have a mean deviation of 0.0726 and a root mean square error of 0.0600. The larger scatter of q values at low S reflect the larger experimental uncertainties due to smaller amplitude ratios and phase offsets for this range. The recovery of q values from the phase offset is less accurate due to the exponential amplification of the deviations in the phase term, even though the direct effect of the tether on the phase offset is more clearly detectable.

The solutions of both equations above can be obtained by following the same method as for the Basset drag with the half-order derivative, as detailed in § 2.2. For convenience, we note the identity (see Podlubny 1999, p. 311)

$$\mathcal{D}^q \mathrm{e}^{\mathrm{i}\omega t} = \mathrm{e}^{\mathrm{i}q\pi/2}\omega^q \mathrm{e}^{\mathrm{i}\omega t}, \tag{3.23}$$

which is useful in inverting the solution to recover the experimental values of q. With these results, it is possible to determine the order q of the Basset derivative that best satisfies the experimental data for the whole range of parameters under study.

Solving (3.21) and (3.22) with the order of derivative q as the single unknown parameter, we determine the value of q that minimizes the error in the experimental data. The results are presented in figure 12, which clearly shows, with very little scatter, that the order of the Basset drag is equal to $1/2$ for $S > 1$. The Basset form of the history drag is very strongly validated, even for values of S slightly smaller than unity, although the scatter in the data is much larger in this range because both the amplitude ratio and the phase offset are smaller when $S < 1$. Smaller values of η and ϕ imply larger experimental uncertainty.

4. Conclusions

A detailed model that captures the dynamics of a particle–tether system for small-amplitude oscillations in a viscous fluid is presented. In the mathematical formulation of the problem, the particle equation of motion plays the role of a boundary condition for the tether equation of motion. For the stationary solution under harmonic forcing, the system degenerates into an ODE that is readily solvable analytically. If the tether is both thin and long enough in comparison to the particle radius, its effect on the particle motion can be neglected for small-amplitude oscillations at high frequencies

($S > 1$). Even relatively large deviations in the physical properties and dimensions of the tether used in the experiments of L'Espérance *et al.* (2005) have little effect on the particle dynamics when compared with the free-particle solution.

At frequencies approaching the limit as the viscous time scale (a^2/ν) approaches the flow time scale ($9/\Omega$), i.e. when $S = Sl\,Re_p \sim 1$, tether effects are still small but measurable, especially for light particles. The few experimental results available in this range validate the tethered-particle model, showing that the tether dynamics advanced in the present work is verifiable.

The functional form of the history drag for small but finite Re_p is well represented by the classical Basset drag as an exact half-derivative of the relative velocity for a wide range of values of $Re_p < 1$, as long as $Sl \geqslant 1$. The larger experimental errors due to smaller amplitude ratios and smaller phase offsets that characterize the regime $S < 0.5$ preclude a conclusive validation of the form of the history kernel for lower values of S, but the error incurred by assuming the exact $1/2$ order is relatively small for any value of $S > 0.5$. The range of frequencies characterized by $S < 0.5$ is where the assumption of low Re_p and high $S = Sl\,Re_p$ breaks down, so extrapolations into smaller values of S should be made cautiously. In the range of validity of the theory, the dynamics and shape of the tether are more complex for light particles due to the larger displacements.

The analytical model developed in this work for the tethered-particle motion allows the experimentalist to select experimental parameters for a variety of different goals, and to concentrate on the optimization of the parameters that yield greater effects on the particle motion. Tether thickness and density effects are secondary to tether length. For example, if the goal of the experiment is to minimize tether effects, using values of $\epsilon_r > 3000$ guarantees that tether effects will be minimal for any value of $S > 0.5$, even for the more sensitive phase offset of lighter particles. If the objective is to study history effects at $S \sim 1$, light particles with larger values of ϵ_r are recommended because experimental uncertainties are minimized when larger phase offsets and amplitude ratios are present. If the objective is to study tethered-particle dynamics, smaller values of ϵ_r (of the order of 1000) should be used.

Acknowledgements

The authors gratefully acknowledge the experimental team at MetroLaser Inc., in particular Drew L'Esperance, Mike Dempsey and James D. Trolinger, for the detailed high-speed experiments conducted for NASA's flight definition project SHIVA (Spaceflight Holography Investigation in a Virtual Apparatus) under contract number NAS9-98091. Fruitful discussions with the entire SHIVA team, particularly with William K. Witherow of NASA MSFC and Roger H. Rangel of UC Irvine, are also acknowledged.

REFERENCES

ABBAD, M. & SOUHAR, M. 2004 Experimental investigation on the history force acting on oscillating fluid spheres at low Reynolds number. *Phys. Fluids* **16**, 3808–3817.

BASSET, A. B. 1888 On the motion of a sphere in a viscous liquid. *Phil. Trans. R. Soc. Lond.* A **179**, 43–63.

BOUSSINESQ, J. 1885 Sur la résistance qu'oppose un liquide indéfini en repos, sans pesanteur, au mouvement varié d'une sphère solide qu'il mouille sur toute sa surface, quand les vitesses restent bien continues et assez faibles pour que leurs carrés et produits soient négligeables. *C. R. Acad. Sci. Paris* **100**, 935–937.

CANDELIER, F., ANGILELLA, J. R. & SOUHAR, M. 2004 On the effect of the Boussinesq-Basset force on the radial migration of a Stokes particle in a vortex. *Phys. Fluids* **16**, 1765–1776.

CANDELIER, F. & SOUHAR, M. 2007 Time-dependent lift force acting on a particle moving arbitrarily in a pure shear flow, at small Reynolds number. *Phys. Rev.* E **76**, 067301.

CHAO, B. T. 1968 Turbulent transport behaviour of small particles in dilute suspension. *Ósterreich. Ing.-Arch.* **18**, 7–21.

COIMBRA, C. F. M. 2003 Mechanics with variable-order differential operators. *Ann. Phys.* **12**, 692–703.

COIMBRA, C. F. M. & KOBAYASHI, M. H. 2002 On the viscous motion of a small particle in a rotating cylinder. *J. Fluid Mech.* **469**, 257–286.

COIMBRA, C. F. M., L'ESPÉRANCE, D., LAMBERT, R. A., TROLINGER, J. D. & RANGEL, R. H. 2004 An experimental study on stationary history effects in high-frequency Stokes flows. *J. Fluid Mech.* **504**, 353–363.

COIMBRA, C. F. M. & RANGEL, R. H. 1998 General solution of the particle momentum equation in unsteady Stokes flow. *J. Fluid Mech.* **370**, 53–72.

COIMBRA, C. F. M. & RANGEL, R. H. 2001 Spherical particle motion in harmonic Stokes flows. *AIAA J.* **39** (9), 1673–1682.

HINZE, J. O. 1975 *Turbulence*. McGraw-Hill.

HJELMFELT, A. T. & MOCKROS, L. F. 1966 Motion of discrete particles in turbulent fluid. *Appl. Sci. Res.* **16**, 148–161.

HWANG, W. T. & EATON, J. K. 2006 Homogeneous and isotropic turbulence modulation by small heavy ($St \sim 50$) particles. *J. Fluid Mech.* **564**, 361–393.

KIM, I., ELGHOBASHI, S. E. & SIRIGNANO, W. A. 1998 On the equation of motion for spherical-particle motion: effects of Reynolds and acceleration numbers. *J. Fluid Mech.* **367**, 221–253.

L'ESPÉRANCE, D., COIMBRA, C. F. M., TROLINGER, J. D. & RANGEL, R. H. 2005 Experimental verification of fractional history effects on the viscous dynamics of small spherical particles. *Exp. Fluids* **38**, 112–116.

L'ESPÉRANCE, D., TROLINGER, J. D., COIMBRA, C. F. M. & RANGEL, R. H. 2006 Particle response to low-Reynolds-number oscillation of a fluid in microgravity. *AIAA J.* **44**, 1060–1064.

MEI, R. W. & ADRIAN, R. J. 1992 Flow past a sphere with an oscillation in the free-stream velocity and unsteady drag at finite Reynolds number. *J. Fluid Mech.* **237**, 323–341.

MEI, R. W., LAWRENCE, C. J. & ADRIAN, R. J. 1991 Unsteady drag on a sphere at finite Reynolds number with small fluctuations in the free-stream velocity. *J. Fluid Mech.* **233**, 613–631.

MORRISON, F. A. & STEWART, M. B. 1976 Small bubble motion in an accelerating fluid. *J. Appl. Mech.* **97**, 399–402.

PEDRO, H. T. C., KOBAYASHI, M. H., PEREIRA, J. M. C. & COIMBRA, C. F. M. 2008 Variable order modeling of diffusive-convective effects on the oscillatory flow past a sphere. *J. Vib. Control* **14**, 822–827.

PODLUBNY, I. 1999 *Fractional Differential Equations*. Academic Press.

SHERMAN, F. S. 1990 *Viscous Flow*. McGraw-Hill.

TCHEN, C. M. 1947 Mean value and correlation problems connected with the motion of small particles suspended in a turbulent fluid. Doctoral dissertation, Delft University, The Hague.

WEINSTEIN, J. A., KASSOY, D. R. & BELL, M. J. 2008 Experimental study of oscillatory motion of particles and bubbles with applications to Coriolis flow meters. *Phys. Fluids* **20**, 103306.